APL Photonics

Ultra-compact visible chiral spectrometer with meta-lenses

Cite as: APL Photonics **2**, 036103 (2017); https://doi.org/10.1063/1.4974259
Submitted: 04 November 2016 . Accepted: 05 January 2017 . Published Online: 07 February 2017

Alexander Y. Zhu, Wei-Ting Chen, Mohammadreza Khorasaninejad, Jaewon Oh, Aun Zaidi, Ishan Mishra, Robert C. Devlin, and Federico Capasso

APL PHOTONICS **2**, 036103 (2017)

Ultra-compact visible chiral spectrometer with meta-lenses

Alexander Y. Zhu,[1,a] Wei-Ting Chen,[1,a] Mohammadreza Khorasaninejad,[1]
Jaewon Oh,[1,2] Aun Zaidi,[1] Ishan Mishra,[1,2] Robert C. Devlin,[1]
and Federico Capasso[1,b]
[1]*Harvard John A. Paulson School of Engineering and Applied Sciences, Harvard University, Cambridge, Massachusetts 02138, USA*
[2]*University of Waterloo, Waterloo, Ontario N2L 3G1, Canada*

(Received 4 November 2016; accepted 5 January 2017; published online 7 February 2017)

Conventional compact spectrometers have a fixed spectral resolution and cannot resolve the polarization properties of light without additional optical elements, while their larger counterparts are bulky and costly. Here, we demonstrate multiple off-axis meta-lenses in the visible integrated on a single planar substrate. They possess both focusing and strongly dispersive properties and are designed to provide different spectral resolutions as well as working wavelength ranges on the same chip. We realize a compact spectrometer using only these meta-lenses and a CMOS camera and achieve detector-limited spectral resolutions as small as 0.3 nm and a total working wavelength range exceeding 170 nm for a beam propagation length of only a few cm. In addition, this spectrometer has the capability to resolve different helicities of light in a single measurement. This chip-camera setup represents the most compact configuration so far achieved for a spectrometer with similar performance and functionality, and its compatibility with large-scale fabrication processes makes it broadly applicable. [http://dx.doi.org/10.1063/1.4974259]

I. INTRODUCTION

Recent advances in nanoscience have led to the development of new technologies for diverse areas of applications, ranging from disease diagnostics to environmental monitoring and energy storage.[1–4] Its broad appeal is centered on three aspects: improvement in performance, miniaturization and reduction of system complexity, and addition of new functionalities. In the context of optics, the development of metasurfaces comprising of sub-wavelength scatterers at an interface[5,6] has given rise to an impressive host of applications ranging from planar lenses,[7–12] wave-plates,[13] holograms,[14–18] beam deflectors[19–24] to even cloaking[25] and analog computing devices.[26]

On a system level, a basic but essential tool for many optical instruments is the spectrometer. The ability to decode changes to the spectrum of light in response to external stimuli is central to applications such as environmental monitoring of pollutants and the detection of specific antibodies in disease diagnostics.[1–4] Furthermore, advanced techniques such as circular dichroism spectroscopy are widely used to obtain additional circular polarization (CP) information in order to distinguish between optical isomers during the manufacture of many pharmaceutics and agrochemicals.[27,28]

Conventional approaches to acquire spectral and circular polarization information require cascading multiple components such as non-polarizing beam splitters, waveplates, and polarizers, or composite prisms comprised of naturally birefringent crystals (e.g., Fresnel rhomb)[29] paired with a spectrometer. These spectrometers usually consist of focusing mirrors and a grating turret.[30] They suffer from insufficient grating dispersion to allow for large spatial separation within a short (e.g., mm to cm) light propagation distance, which places a lower limit on their physical size in order to

---

[a] A. Y. Zhu and W. T. Chen contributed equally to this work.
[b] Author to whom correspondence should be addressed. Electronic mail: capasso@seas.havard.edu

achieve sufficient spectral resolution. The necessity of using a turret to mount gratings with different dispersions in order to tune/adjust spectral resolutions also adds significant complexity and bulkiness to the system. While handheld and miniaturized spectrometers do indeed exist,[31–34] they are typically limited to a single, fixed spectral resolution and lack polarimetric capabilities. Similarly, while there have been efforts to utilize metasurfaces for spectroscopy, these devices typically suffer from these same limitations or a low spectral resolution.[35–37]

These are strong motivations to develop compact spectrometers capable of good spectral performance and helicity-resolving capabilities, i.e., distinguishing right/left circularly polarized (RCP/LCP) light. Recently we have demonstrated silicon based off-axis meta-lenses at near-infrared wavelengths.[38] These meta-lenses can provide high spectral resolution beyond what is achievable by conventional gratings. However, their efficiency is significantly reduced in the visible range due to intrinsic material losses; additionally they were not designed to provide polarization information. Here we present off-axis meta-lenses operating at visible wavelengths with the added functionality of resolving the helicity of incident light. This is made possible using a recently developed titanium oxide (TiO_2) atomic layer deposition (ALD) process.[39] TiO_2 is lossless across the visible spectrum and possesses a moderately high refractive index to provide strong light confinement. This ALD process enables the fabrication of high quality nano-structures with minimal roughness and vertical sidewall profiles, which are essential to realize highly efficient metasurface devices. Earlier works typically made use of reactive ion etching (RIE) processes which limited the steepness of the sidewall profile and aspect ratio of fabricated structures.[40] This translates into inaccuracies in the resultant phase profile, which can be significant despite having only a small amount of tapering.[41] By integrating multiple off-axis meta-lenses with different parameters (focal length, spatial size, position, and focusing angle) onto the same substrate, a highly versatile ultra-compact spectrometer with variable resolution, spectral range, and minimal spatial footprint can be achieved. Due to the intrinsic CP sensitivity of meta-lenses based on the geometric phase, such a spectrometer is also capable of resolving the helicity of light in a single measurement. We call it a chiral spectrometer by virtue of this functionality. Finally, their CMOS-compatible fabrication process is amenable to monolithic integration with camera sensors and large-scale production.

II. DEVICE DESIGN

A. Meta-grating design

The building block of all metasurface elements in this work is a TiO_2 nanofin on a glass substrate (Fig. 1(a)) which acts as a birefringent waveguide. Phase control is achieved by geometric rotation of the nanofins, resulting in phase acquisition equal to twice the rotation angle (Pancharatnam-Berry phase).[42,43] The latter is accompanied by a conversion of the incident light helicity. We experimentally and numerically demonstrate this concept by first designing a meta-grating. A scanning electron microscope (SEM) image is shown in Fig. 1(b). The meta-grating diffracts the incident light into the $+1$ and -1 orders for RCP and LCP, respectively. The diffraction angle follows that of a conventional grating $\sin^{-1}(\lambda/P)$, where λ is the wavelength and P is the period. Here the design wavelength for maximum conversion efficiency was determined to be 500 nm, and the period was 1 μm. Efficiencies as high as 70% and extinction ratios up to 16 dB were measured in the vicinity of the design wavelength, as shown in Fig. 1(c). We observe a difference (particularly at shorter wavelengths) between the experimental and simulated efficiency curves due to deviations in the size of the nanostructures from the intended design. This likely arises from the fabrication process, such as proximity effects during electron beam lithography, which cause the peak efficiency to be redshifted compared to the simulation. The efficiency is defined as the ratio of optical power in the desired order to that of incident light. The latter is measured after passing it through an aperture of the same size as the grating (here 250 μm × 250 μm) on the same substrate. The extinction ratio is calculated as the ratio of measured power for two different helicities of light in the same diffracted order. We also theoretically studied the dependence of the efficiency with grating period for the same nanofin parameters, where the unit cell and nanofin sizes are kept constant (Fig. 1(d)). As expected from the Nyquist sampling criteria, with decreasing grating period (or equivalently, increasing diffraction angle), the efficiency drops since there are less phase levels per period.

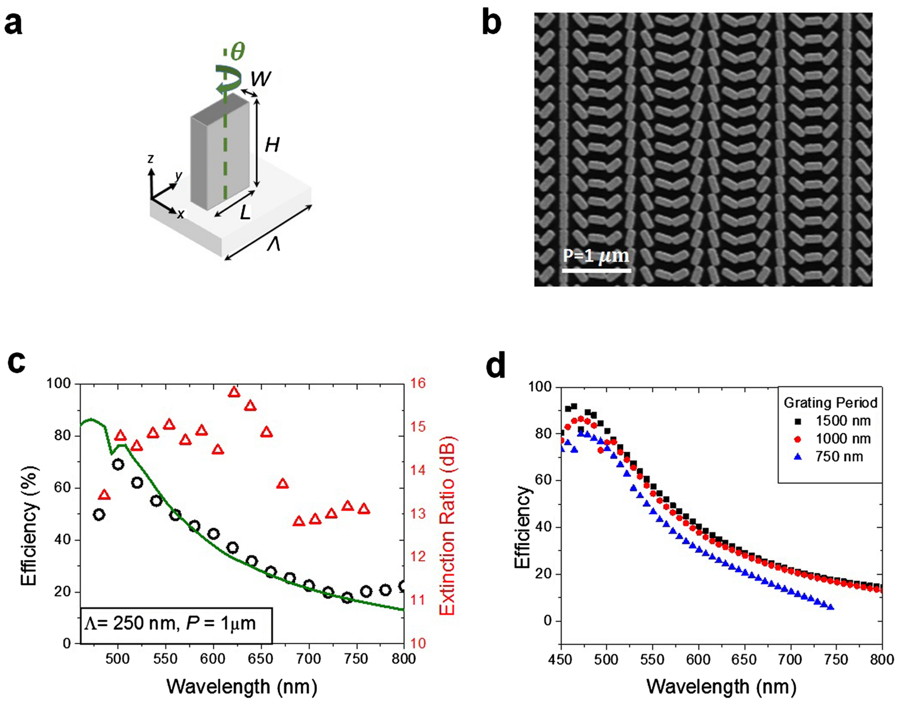

FIG. 1. (a) Schematic of a single nanofin with width W, height H, length L, and unit cell size Λ on a glass substrate. These values are $W = 80$ nm, $H = 600$ nm, $L = 210$ nm, and $\Lambda = 250$ nm for the results shown in (b) and (c). Each nanofin is rotated by an angle θ to impart the desired phase at each spatial location. Coordinate axes are defined with respect to the plane of the structures. (b) Top-view scanning electron microscope image of a meta-grating comprised of arrays of nanofins. Here each period ($P = 1\ \mu$m) comprises 4 phase levels (nanofins). Scale bar: 1 μm. (c) Measured (black circles) and simulated (green line) efficiencies of the +1 order metasurface grating shown in (b) under illumination with right-handed circularly polarized light. Extinction ratio (red triangles) of the meta-grating as a function of wavelength is also plotted. (d) Simulated efficiencies using the same nanofin parameters (W, H, L, and Λ) for different grating periods of 1500 nm, 1000 nm, and 750 nm, corresponding to different deflection angles of 20°, 30°, and 42° at 500 nm.

B. Meta-lens design

So far, we have demonstrated an efficient meta-grating with a chiral response in the visible. However, similar to a conventional grating, in order to enhance spectral resolution, one should place the detector far away from the meta-grating, which makes high resolution spectrometers bulky. The required propagation distance for a given spectral resolution can be substantially reduced by focusing the light that emerges from the meta-grating. This can be achieved by imparting the hyperbolic phase profile of a lens to the nanofins of the metasurface, such that incoming light of a certain wavelength is focused into a diffraction-limited spot (Fig. 2(a)) on the optical axis. The required phase at each point of the meta-lens must follow[38]

$$\varphi(x, y) = 2\pi - \frac{2\pi}{\lambda_d}\left(\sqrt{\left(x - x_f\right)^2 + \left(y - y_f\right)^2 + z_f^2} - f\right), \tag{1}$$

where $f = \sqrt{x_f^2 + y_f^2 + z_f^2}$ is the focal length, and φ and λ_d are the required phase and design wavelength, respectively. All coordinates and phases are defined with respect to the center nanofin ($x = 0$, $y = 0$, $z = 0$). Equation (1) compensates for the phase shifts between the varying optical paths of light originating from different positions on the meta-lens such that constructive interference takes place at the focus (x_f, y_f, z_f). The method of implementation of this phase mask is again through the use of rotated nanofins whose parameters are identical to that used for the meta-grating. This rotation results in acquisition of a geometric phase equal to twice the rotation angle. Note that for a given phase profile of a meta-lens, Eq. (1) indicates that its focal length changes strongly as a function

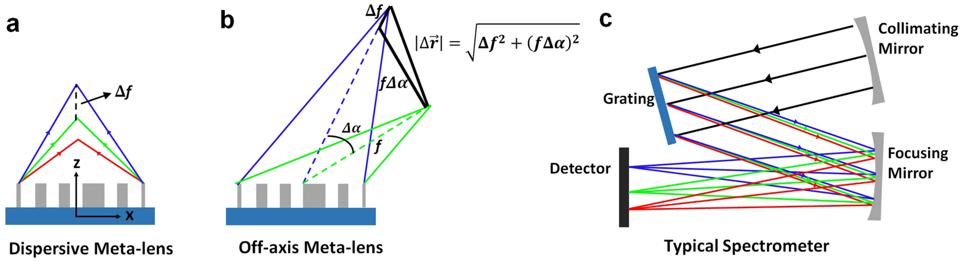

FIG. 2. (a) Schematic showing that a meta-lens whose phase profile is given by Equation (1) is chromatically dispersive, i.e., the focal length changes as a function of wavelength. The colors of the rays represent their respective wavelengths (red, green, and blue). (b) Schematic diagram for an off-axis meta-lens. The focusing angle also changes with wavelength in addition to the longitudinal focal length shift. They both contribute to the transverse displacement of the focal spot $|\Delta\vec{r}|$ along a given plane. (c) Schematic illustration of operation of a conventional grating spectrometer. The focusing and dispersive (grating) elements are separated. By design, the focusing mirror is achromatic and light with different wavelengths is focused onto the same detector plane, with lateral displacement resulting solely from the grating dispersion.

of wavelength, i.e., the focal spot undergoes a longitudinal displacement Δf along the optical axis (Fig. 2(a)). In addition, one can design an off-axis meta-lens using Eq. (1) by placing the focal spot at $x_f = f\sin(\alpha)$, $y_f = 0$, and $z_f = f\cos(\alpha)$, where α is the angle between the line from the center of meta-lens to the focal spot and the vertical axis, defined as the focusing angle. When α is non-zero, a small change in the wavelength of incident light results in an additional *lateral* displacement of the focal spot $f\Delta\alpha$ whose magnitude is strongly dependent on both f and α. The resultant sum $|\Delta\vec{r}|$ of these displacements is shown in Fig. 2(b); its variation with wavelength can be quantified via the dispersion $\frac{|\Delta\vec{r}|}{\Delta\lambda}$ along an appropriately placed camera plane,

$$\frac{|\Delta\vec{r}|}{\Delta\lambda} = \sqrt{\left(\frac{\Delta f}{\Delta\lambda}\right)^2 + f^2\left(\frac{\Delta\alpha}{\Delta\lambda}\right)^2}, \tag{2}$$

where $\Delta\alpha$ represents change in the focusing angle due to a small wavelength change $\Delta\lambda$.

Compared to conventional grating spectrometers (Fig. 2(c)) whose focusing elements are achromatic due to the use of reflective optics, the aforementioned longitudinal focal length change of the off-axis meta-lenses can be exploited to further increase the dispersion of a compact spectrometer. In conventional spectrometers, the focal length change is negligible so that any contribution to the dispersion arises solely from the change in grating diffraction angle. Furthermore, in conventional gratings, the diffraction angle is limited to approximately a few tens of degrees, due to shadowing effects. These factors significantly limit the dispersion that can be achieved in such spectrometers.

The minimum resolvable wavelength difference $\delta\lambda_{min}$ (spectral resolution) at the design wavelength λ_d corresponds to a focal spot displacement given by the Rayleigh criterion, i.e.,

$$\delta\lambda_{min} = \Delta\lambda/|\Delta\vec{r}| \times 0.61\lambda_d/NA, \tag{3}$$

where $\Delta\lambda/|\Delta\vec{r}|$ is the reciprocal dispersion which can be obtained from Eq. (2) and NA is the numerical aperture of the off-axis meta-lens. However, in a spectrometer, the pixel size of the camera introduces a further constraint on the spectral resolution since the pixel size defines the sampling rate. If the pixel size is large compared to $\frac{0.61\lambda_d}{NA} \times 1/2$, according to the Nyquist sampling theorem, aliasing occurs, which prevents the resolving of two points in close proximity. Since in general at least three pixels are required to distinguish two points, the final spectral resolution of the spectrometer at the design wavelength is the convolution between these two effects and can be written as[38]

$$\delta\lambda_{min} = \Delta\lambda/|\Delta\vec{r}| \times \frac{0.61\lambda_d}{NA} + \Delta\lambda/|\Delta\vec{r}| \times 3D/M, \tag{4}$$

where D and M are the camera pixel size and magnification of the spectroscopic imaging system, respectively. From this discussion, it is evident that by tailoring the off-axis focusing angle as well as the focal length, one can achieve a desired dispersion (Eq. (2)), and hence spectral resolution, at any design wavelength using meta-lenses. However, there is a trade-off between the spectral resolution and spectral range. For a system with a fixed detector size, using a higher NA meta-lens for a higher spectral resolution results in more chromatic aberration (e.g., broadening of the focal spot size) for a given change in wavelength, which limits the spectral range of the spectrometer. Another challenge associated with using high NA lenses is to locate a common plane where multiple wavelengths are in focus, due to the smaller depth of focus. Alternatively, one can lower the NA while increasing the dispersion to maintain similar resolution for a wider spectral range. In this case, since the dispersion is larger, the area of the active region of the camera sensor will pose the final limit to the working wavelength range.

III. CHARACTERIZATION

A. Meta-lenses

For general spectroscopic applications, which require a large working wavelength range and high resolving power within a spectrum of interest, we integrate several off-axis meta-lenses on the same substrate to provide spatially separated focal spots in the same field of view of a camera. Each meta-lens possesses different spectral resolutions and spectral ranges and selectively focuses light with opposite CP states. In this way, we can realize in a single device within an area of less than 2 cm × 1 cm, the equivalent of multiple distinct gratings (with different wavelength ranges and resolutions), focusing lenses, and CP elements.

A representative SEM image of an off-axis meta-lens is shown in Fig. 3(a). For the final device (Fig. 3(b)), we fabricated four meta-lenses: two at large ($\alpha = 60°$) focusing angles with a NA of 0.1 for high spectral resolution (R1 and L1) and two at small focusing angles of 25° with a NA of 0.022 for a larger spectral range (R2 and L2). The two meta-lenses fabricated for each NA are sensitive to opposite helicities of incident circularly polarized light: as a result of the use of the geometric phase in the design, any one single meta-lens would focus light of a chosen handedness while defocusing the other. Note that these meta-lenses are designed according to the phase profile dictated by Equation (1), with care taken to avoid spatial overlapping of focal spots from different meta-lenses by proper placement on the substrate. The final shape of our meta-lenses is rectangular instead of circular to keep the focal spots within the active region of the camera; this results in the asymmetrical shape of the focal spots. The primary focusing/dispersion direction is along the horizontal axis of Fig. 3(c).

We first characterized the focal spots using a narrow line width (~pm) diode laser (Quantum Optics) at the design wavelength of 532 nm. The laser beam is coupled into a fiber and subsequently collimated (Thorlabs RC04APC-P01) before being incident on the meta-lenses. An objective lens (Mitutoyo M Plan Apo 10×, NA 0.28) paired with a tube lens of focal length f = 200 mm and a CMOS camera (Edmund EO-5012) with a small pixel size of 1.67 μm were used for accurate characterization. Measured results are in good agreement with theory: we observe close to diffraction limited focal spots with full-width half maximum (FWHM) of 2.3 μm and 11.6 μm for the high and low NA meta-lenses, respectively (Figs. 3(c) and 3(d)). Similar values were obtained for meta-lenses designed for the opposite helicity. Additionally, we observe from Fig. 3(c) that the divergent light of opposite helicity introduces negligible background noise to the system.

B. Meta-spectrometer

To build a compact spectrometer, we paired the meta-lenses with a CMOS camera (Thorlabs DCC1545M) (Fig. 4(a)). It has a pixel size of 5.2 μm and an active area of 6.66 × 5.32 mm^2. The camera plane is placed so that the quality of the focal spots (i.e., shape and symmetry) is optimized for two distinct wavelengths (λ = 532 nm and λ = 660 nm). The images of the focal spots corresponding to the NA = 0.1 and NA = 0.02 meta-lenses under linearly polarized light at λ = 532 nm, as well as their horizontal cuts, are shown in Fig. 4(b). Note that here the FWHM of the focal spot profiles are limited by the camera's pixel size, in contrast to the characterization shown in Fig. 3(c).

One often cited concern about metasurface focusing and dispersive elements is chromatic aberration. Since the required phase profile is wavelength dependent, at wavelengths different from the design, the focal spot will be aberrated and its position will be shifted both laterally and longitudinally (along the focusing axis). These aberrations are more pronounced for higher NA lenses due to the

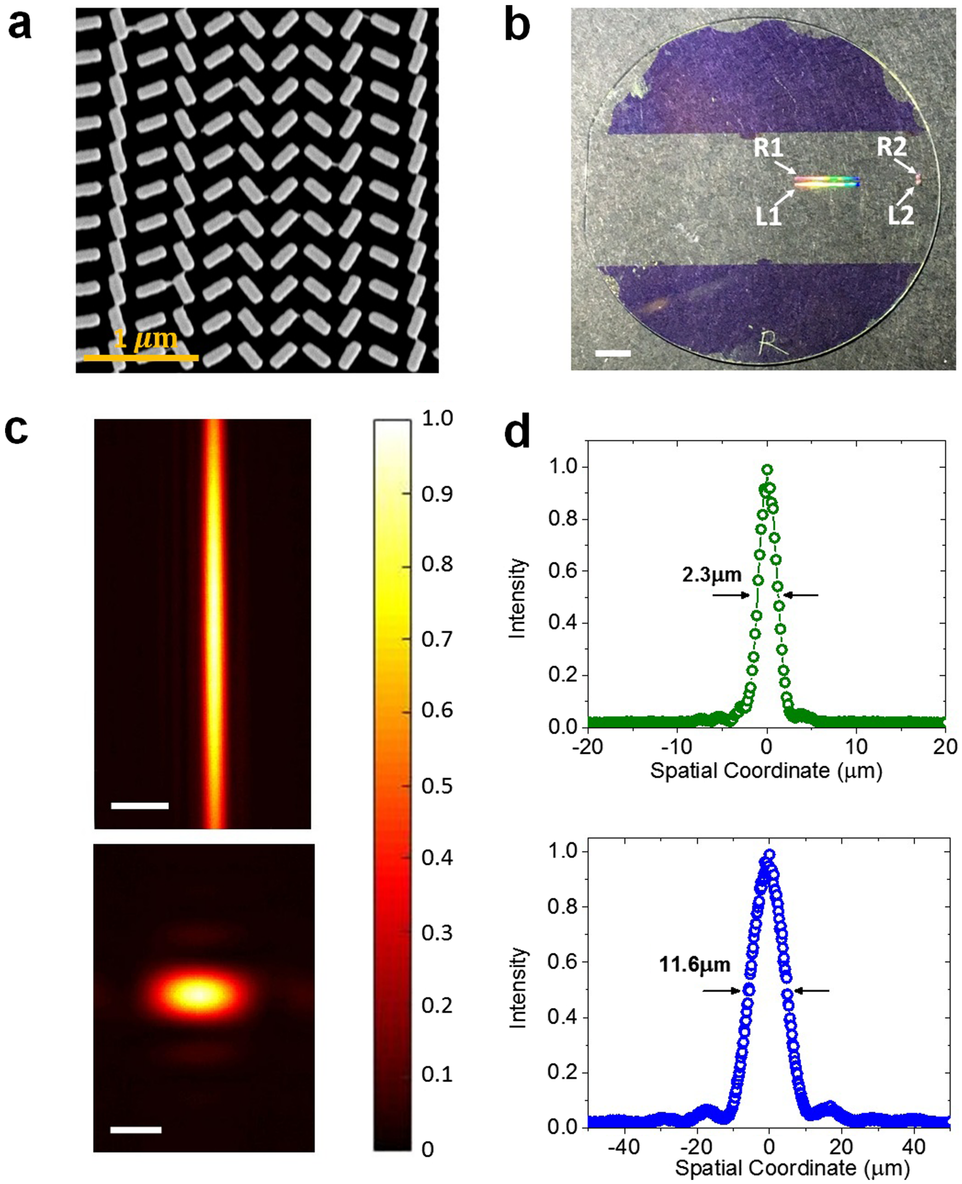

FIG. 3. (a) Scanning electron microscope image of a fabricated off-axis meta-lens. (b) Photograph of a fabricated device with four separate meta-lenses labeled R1, R2, L1, and L2. These meta-lenses are designed based on the phase profile in Eq. (1) but rectangular in shape to keep all focal spots within the active region of the camera. The primary focusing/dispersion direction is along the horizontal axis of the image. The letters R and L refer to the helicity of light focused by each meta-lens; 1 and 2 indicate the parameters used for the lens design. R1 and L1 have a NA of 0.11, focusing angle $\alpha = 60°$, and a focal length of 20.1 mm, while R2 and L2 have an NA of 0.022, focusing angle of $\alpha = 25°$, and a focal length of 11.1 mm. Physical dimensions of the lenses are 9×0.1 mm (R1 and L1) and 0.5×0.8 mm (R2 and L2). Scale bar: 5 mm. (c) CMOS camera image after magnification using a 10× objective of the focal spots generated by the meta-lenses for circularly polarized incidence. The upper and bottom focal spot corresponds to meta-lens R1 and R2. Both scale bars: 25 μm. (d) Horizontal cuts of the focal spots in (c), showing diffraction limited focusing.

smaller focal spot size. In general, in order to maintain high spectral resolution for as wide a range of wavelengths as possible, the focal spot quality (i.e., its size and shape) should be preserved for that range. This requires both a suitable NA in terms of lens design and appropriate placement of the detector plane such that it intersects with the focal spots within their depth of focus. Here, we specifically designed the small diameter meta-lenses (labelled R2 and L2 in Fig. 3(b)) for a large spectral range while maintaining a reasonable spectral resolution. Ray-tracing simulations of their

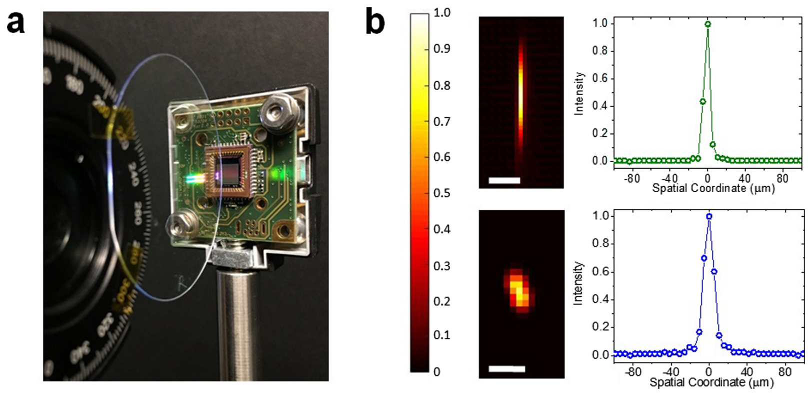

FIG. 4. (a) Photograph of the meta-spectrometer consisting of meta-lenses and a camera. (b) Measured intensity profiles of focal spots of (left) and their corresponding horizontal cuts (right) from the camera shown in (a), under linearly polarized light from a diode laser at $\lambda = 532$ nm. Top and bottom panels correspond to the focal spots of the NA = 0.1 and NA = 0.02 lenses, respectively. Scale bars: 40 μm (top) and 30 μm (bottom).

performance at 470 nm, 532 nm, and 660 nm are shown in Fig. 5(a). These simulations provide a guideline to identify the optimal position of the camera plane for minimizing the focal spot simultaneously at different wavelengths within the working range. This range is defined as the spectrum over which the focal spots are still close to diffraction-limited along the dispersion direction. This criterion is more stringent than typically used in the industry, but we nevertheless find, under this definition, the spectral range of our meta-lenses to be almost 200 nm.

The aforementioned focal spot sizes are computed using a commercial software OpticStudio (Zemax LLC). Figures 5(b)–5(d) show the spot diagrams corresponding to the intercept points on the camera plane (black dashed line in Fig. 5(a)) for rays passing through the meta-lens. The colors of the spots correspond to their wavelength, i.e., 470 nm (blue), 532 nm (green), and 660 nm (red). To visualize the spreading of the points, the ideal Airy disk at each chosen wavelength is plotted as a reference. These were calculated by using the Huygens–Fresnel principle to propagate the complex electric fields at the meta-lens to its corresponding focal plane. For wavelengths away from the design wavelength $\lambda_d = 532$ nm, the focal plane is defined by a normal vector and a point, corresponding to the propagation direction of the chief ray (the normal vector) as well as the intersection of the chief ray and paraxial rays (the point). This definition was used in the calculations since due to chromatic aberrations, not all rays have a common intersection at wavelengths different from the design wavelength. From Figs. 5(b)–5(d), it is clearly seen that the focal spots within 470–660 nm lie mostly within their Airy disk along the dispersion direction. Deviations are within the pixel size of our camera (5.2 μm). Note that this only applies to the primary focusing direction of the meta-lenses (horizontal axis in Figs. 5(b)–5(d)).

Subsequently, we used a supercontinuum laser (SuperK Varia, NKT photonics) with its bandwidth set to 5 nm for wavelengths ranging from 480 nm to 780 nm in steps of 10 nm to characterize the performance of our meta-spectrometer and compare it against that of a commercial handheld spectrometer (OceanOptics USB4000 UV-VIS). The known center wavelengths of the supercontinuum laser input are used to calibrate our system and account for the slight non-linear dispersive effects across this broad wavelength range (Fig. S1 of the supplementary material). Figures 5(e) and 5(f) illustrate the measured spectrum by the meta-spectrometer and the commercial spectrometer, respectively. Camera images of the focal spots are shown in Figure S2. We observe close to identical spectral lineshapes with FWHM between 5 and 8 nm across the visible. This validates the claim for the working range of the low NA meta-lenses; additionally, we do not observe any significant linewidth broadening effects with the increase in wavelength within our previously defined working wavelength range from 470 nm to 660 nm. Beyond this range, due to aberrations in the focal spots, one can observe a significant, consistent increase in FWHM which is larger than the commercial system (Figure S3 of the supplementary material). This is in good agreement with our previously discussed theoretical results in Figs. 5(b)–5(d). These results also offer further evidence[9,10,38] that by a proper design a planar meta-lens can achieve comparable or even superior performance to traditional lenses.

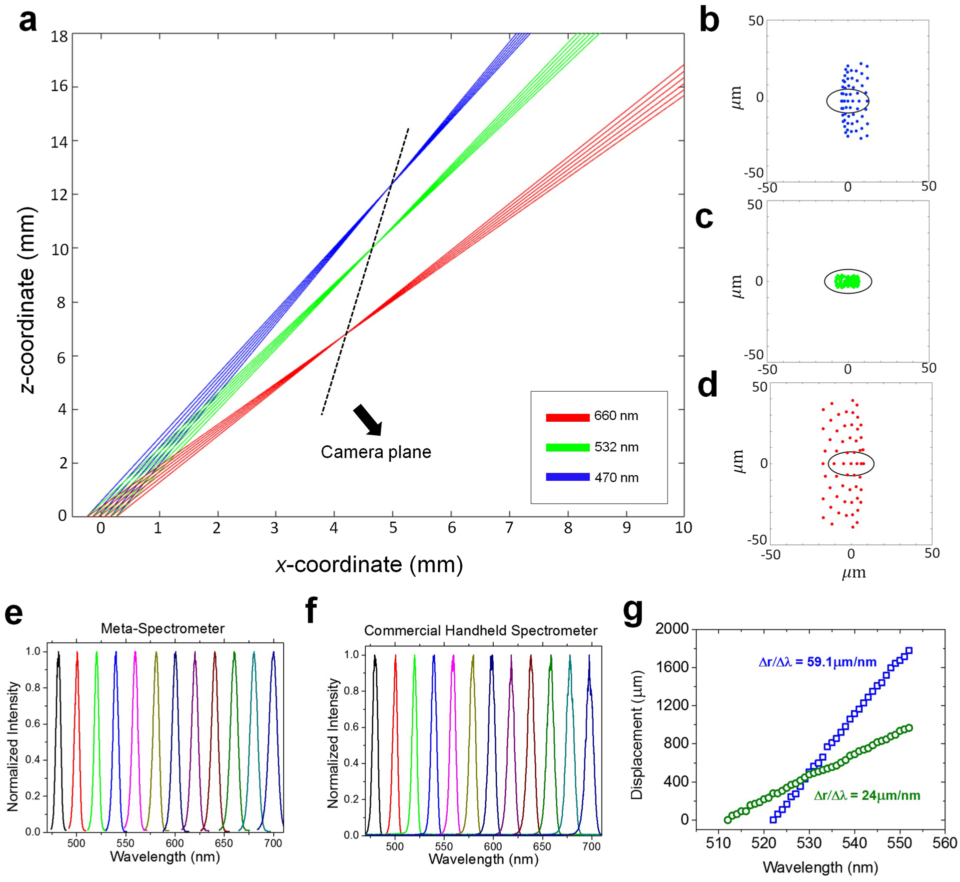

FIG. 5. (a) Ray tracing calculations for the low NA meta-lenses (R2 and L2 in Fig. 3(b)), which were designed for $\lambda = 532$ nm, at wavelengths of 470 nm, 532 nm, and 660 nm. A plane which simultaneously intercepts the focal planes at each of these wavelengths is shown. (b)–(d) Simulated spot diagrams color-coded to match their corresponding wavelengths. The ideal, aberration-free Airy disks are plotted as a reference. Good focal spot quality is preserved over a large wavelength range. (e) Measured spectra from a supercontinuum laser with 5 nm bandwidth using the meta-lens spectrometer, and (f) a commercial handheld spectrometer. The center wavelengths used varied from 480 nm to 700 nm in increments of 20 nm. (g) Measured dispersion values for the NA = 0.1 (blue) and NA = 0.02 (green) meta-lenses about their design wavelength of 532 nm.

We next quantified the dispersion and thus the spectral resolution of the meta-spectrometer. Figure 5(g) plots the measured peak intensity positions of the focal spots as a function of wavelength for both high and low NA meta-lenses about their design wavelength of 532 nm. These dispersion values are calculated by tracking the change in these positions as the wavelength is varied with higher precision in steps of 1 nm. As expected and consistent with the earlier calibration results in Fig. S1 of the supplementary material, the observed dispersions are approximately linear within a range of 30-40 nm. We find their values to be 59 μm/nm and 24 μm/nm for meta-lenses with NA of 0.1 and 0.022, respectively. Using Eq. (3), we determine the intrinsic experimental spectral resolution achievable to be 0.05 nm and 0.46 nm for meta-lenses with corresponding NAs of 0.1 and 0.022. In practice, for this meta-lens spectrometer, the spectral resolution is limited by the pixel size of the camera (5.2 μm); the detector-limited attainable spectral resolution therefore becomes (Eq. (4)) 0.31 nm and 1.11 nm, respectively. It is important to note that the values achieved here are a proof of concept, given various experimental constraints. In principle, by using a suitable camera with a larger active region, one can significantly improve the working range while retaining high spectral resolution. As an example, it is possible to design meta-lenses of similar sizes (R2 and L2 in Fig. 3) with a spectral range covering the entire visible (400-800 nm) where all the focal spots lie within their respective diffraction limited Airy disk. Further details and simulated results are presented in Fig. S4 of the supplementary material.

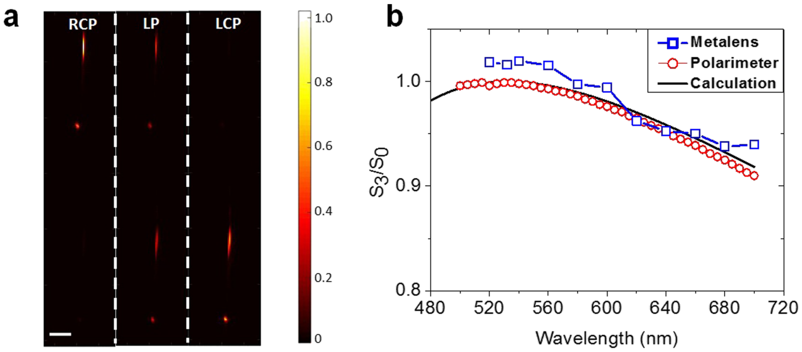

FIG. 6. (a) Stitched camera images of the focal spots from the meta-lenses for right circular polarized (RCP), linearly polarized (LP), and left circularly polarized (LCP) incident light. Intensities are normalized to the same color scale and the illumination wavelength was 532 nm. The intensities of the RCP and LCP spots are observed to be slightly different due to fabrication imperfections as they are focused by different meta-lenses. Scale bar: 100 μm. (b). Normalized S_3/S_0 Stokes parameter as a function of wavelength measured by the meta-spectrometer (blue), a commercial polarimeter (red), and theoretical calculation (black) from the known waveplate retardance.

IV. POLARIZATION INFORMATION

Finally we characterize the CP resolving capability of the meta-spectrometer. A complete description of any arbitrary polarization state can be made using the Stokes parameters S_0, S_1, S_2, and S_3 which correspond to the intensities of incident, vertically polarized, 45° polarized, and circularly polarized light, respectively. Here, we focus on S_3 because the chiral optical response (circular dichroism) of most materials is weak compared to its linear counterpart. Furthermore, conventional approaches to measuring S_3 as a function of wavelength using a single planar device are challenging due to the requirement of separating light in both spectral and polarization domains. Although various nanostructures are known to behave as miniaturized CP filters, they lack the ability to resolve spectral information.[44–46] By using the off-axis meta-lenses based on rotated nanofins, the resulting phase profile intrinsically focuses one helicity while defocusing the other. This functionality thus enables us to resolve the helicity of incident light in a single measurement by having two separate meta-lenses to focus RCP and LCP on the same chip.

Figure 6(a) illustrates the variations in intensities of the focal spots upon changing incident light polarization (from RCP to linear to LCP). Differences in the intensities of the focal spots for RCP and LCP light arise from fabrication errors since they originate from different meta-lenses (R1 and L1 versus R2 and L2, as shown in Fig. 3(b)). To control the polarization of the incident light, we placed a polarizer (Thorlabs GTH10) and a zero-order single wavelength (532 nm) quarter waveplate (Thorlabs WPQ05M-532) in the collimated beam path right before the meta-lenses. Next, we obtained various S_3 Stokes parameters (normalized to incident light intensity S_0) at different wavelengths using the meta-lenses and compared them to the results of a commercial polarimeter and analytical calculations (Fig. 6(b)). These various elliptically polarized states at different wavelengths are generated by changing the wavelength of input light (SuperK Varia). Due to the deviation in optical retardance of the single wavelength (532 nm) quarter waveplate (characterized and provided by Thorlabs), various elliptical polarization states can be generated across a broad range in the visible. Measured values upon appropriate calibration (following the approach in Ref. 47) are seen to be in good agreement with both the values measured by a commercial polarimeter (Thorlabs TXP) and analytical predictions based on known retardance data. For wavelengths close to $\lambda = 532$ nm where the retardance of the waveplate is almost exactly $\lambda/4$, the measured values are slightly greater than unity (approximately 1.01) likely due to experimental noise (e.g., pixel noise and limited dynamic range of the camera) in the measurements.[48,49] Details of these calculations are provided in Sec. VI. Although here we only obtained S_3/S_0 due to the chiral response of the meta-lenses designed with the geometric phase, in principle, by adding linear grating elements, the full Stokes parameters can be resolved.[50,51]

V. CONCLUSION

In summary, we have demonstrated an ultra-compact meta-spectrometer based on integrating multiple planar off-axis meta-lenses at visible wavelengths. This has several advantages over its traditional grating based counterparts: first, it combines the functions of a focusing and dispersive element in a single planar structure, which eliminates the need for rotating turrets or focusing mirrors. Second, in terms of performance, it surpasses conventional blazed grating elements as one can achieve extremely large dispersions which are otherwise unattainable. In addition, the integration of several meta-lenses with different NAs on one substrate allows for multiple different spectral resolutions and a flexible working wavelength range with no further increase in system bulk or complexity. Finally, the meta-lenses can provide extra information about the circular polarization state of incident light, which is not attainable for conventional devices without the use of additional optical elements (e.g., polarizer and waveplates). The use of dielectric TiO_2 as the working material also renders it compatible with existing CMOS processes where large scale production could take place in a single lithographic step or be monolithically integrated with sensor technologies. We envision numerous potential applications in health care, environmental sensing, and related areas for this technology.

VI. METHODS

A. Calculation of Stokes parameter S_3/S_0

The calculation of the normalized Stokes parameter for circularly polarized light, S_3/S_0, under incident light of an unknown polarization state needs to be calibrated against the spectrometer response for a perfect CP state. However due to waveplate imperfections, typically one obtains an elliptical near-CP state (ENCS) instead.[47] This problem can be resolved by performing two successive calibration measurements using the (imperfect) achromatic quarter waveplate and linear polarizer aligned 45° with respect to each other, where both the waveplate and polarizer are rotated together by 90° in the second measurement. In this case, the averaged intensity (I_{av}) from the two measurements can be shown to be equivalent to the response obtained from a perfect CP state,[47]

$$I_{av} = (I_{ENCS} + I_{ENCS+90^\circ})/2,$$

where I_{ENCS} and $I_{ENCS+90^\circ}$ are the directly measured intensities of the elliptical near-CP states. The intensities are obtained by a simple summation of their corresponding focal spots captured by the camera. The normalized S_{3-cal} is then given by the standard expression,

$$S_{3-cal} = \frac{I_{av-RCP} - I_{av-LCP}}{I_{av-RCP} + I_{av-LCP}},$$

where I_{av-RCP} and I_{av-LCP} are the responses corresponding to the case of RCP or LCP incidence. These S_{3cal} are obtained for wavelengths from 520 nm to 700 nm; they then act as calibration values for the meta-spectrometer. Subsequently, we placed a 532 nm zero-order quarter waveplate after a linear polarizer with their axes aligned 45° with respect to each other. The zero-order quarter waveplate generates elliptical states corresponding to different values of S_3 for various wavelengths due to non-quarter wave retardance at these wavelengths away from 532 nm. The S_3 values are then obtained by measuring the intensity difference of focused LCP and RCP light divided by their intensity summation,

$$S_3 = \frac{I_{RCP} - I_{LCP}}{I_{RCP} + I_{LCP}}.$$

The final calibrated values shown in Fig. 6(b) were obtained by S_3/S_{3-cal} at their corresponding wavelength.

SUPPLEMENTARY MATERIAL

See supplementary material for additional figures (PDF).

ACKNOWLEDGMENTS

This work was supported in part by the Air Force Office of Scientific Research (MURI, Grant Nos. FA9550-14-1-0389 and FA9550-16-1-0156) and Thorlabs, Inc. W.T.C. acknowledges postdoctoral fellowship support from the Ministry of Science and Technology, Taiwan (Grant No. 104-2917-I-564-058). A.Y.Z. thanks Harvard SEAS and A*STAR Singapore under the National Science Scholarship scheme. R.C.D. is supported by a Charles Stark Draper Fellowship. This work was performed in part at the Center for Nanoscale Systems (CNS), a member of the National Nanotechnology Coordinated Infrastructure (NNCI), which is supported by the National Science Foundation under NSF Award No. 1541959. CNS is a part of Harvard University.

[1] H. Zhu, S. O. Isikman, O. Mudanyali, A. Greenbaum, and A. Ozcan, Lab Chip **13**(1), 51–67 (2013).
[2] R. S. Lunetta and C. D. Elvidge, *Remote Sensing Change Detection: Environmental Monitoring Methods and Applications* (Taylor & Francis Ltd., 1999).
[3] A. Voller, D. Bidwell, and A. Bartlett, Bull. W. H. O. **53**(1), 55 (1976).
[4] A. Y. Zhu, F. Yi, J. C. Reed, H. Zhu, and E. Cubukcu, Nano Lett. **14**(10), 5641–5649 (2014).
[5] N. Yu, P. Genevet, M. A. Kats, F. Aieta, J.-P. Tetienne, F. Capasso, and Z. Gaburro, Science **334**(6054), 333–337 (2011).
[6] A. V. Kildishev, A. Boltasseva, and V. M. Shalaev, Science **339**(6125), 1232009 (2013).
[7] F. Aieta, P. Genevet, M. A. Kats, N. Yu, R. Blanchard, Z. Gaburro, and F. Capasso, Nano Lett. **12**(9), 4932–4936 (2012).
[8] M. Khorasaninejad, F. Aieta, P. Kanhaiya, M. A. Kats, P. Genevet, D. Rousso, and F. Capasso, Nano Lett. **15**(8), 5358–5362 (2015).
[9] M. Khorasaninejad, W. T. Chen, R. C. Devlin, J. Oh, A. Y. Zhu, and F. Capasso, Science **352**(6290), 1190–1194 (2016).
[10] M. Khorasaninejad, W. T. Chen, A. Y. Zhu, J. Oh, R. C. Devlin, D. Rousso, and F. Capasso, Nano Lett. **16**(7), 4595–4600 (2016).
[11] D. Lin, P. Fan, E. Hasman, and M. L. Brongersma, Science **345**(6194), 298–302 (2014).
[12] A. Arbabi, Y. Horie, A. J. Ball, M. Bagheri, and A. Faraon, Nat. Commun. **6**, 7069 (2015).
[13] M. Mehmood, S. Mei, S. Hussain, K. Huang, S. Siew, L. Zhang, T. Zhang, X. Ling, H. Liu, and J. Teng, Adv. Mater. **28**(13), 2533–2539 (2016).
[14] M. Khorasaninejad, A. Ambrosio, P. Kanhaiya, and F. Capasso, Sci. Adv. **2**(5), e1501258 (2016).
[15] W. T. Chen, K.-Y. Yang, C.-M. Wang, Y.-W. Huang, G. Sun, I.-D. Chiang, C. Y. Liao, W.-L. Hsu, H. T. Lin, and S. Sun, Nano Lett. **14**(1), 225–230 (2013).
[16] X. Ni, A. V. Kildishev, and V. M. Shalaev, Nat. Commun. **4**, 2807 (2013).
[17] Y.-W. Huang, W. T. Chen, W.-Y. Tsai, P. C. Wu, C.-M. Wang, G. Sun, and D. P. Tsai, Nano Lett. **15**(5), 3122–3127 (2015).
[18] W. Ye, F. Zeuner, X. Li, B. Reineke, S. He, C.-W. Qiu, J. Liu, Y. Wang, S. Zhang, and T. Zentgraf, Nat. Commun. **7**, 11930 (2016).
[19] M. Khorasaninejad and F. Capasso, Nano Lett. **15**(10), 6709–6715 (2015).
[20] C. Ribot, M. S. L. Lee, S. Collin, S. Bansropun, P. Plouhinec, D. Thenot, S. Cassette, B. Loiseaux, and P. Lalanne, Adv. Opt. Mater. **1**(7), 489–493 (2013).
[21] Y. F. Yu, A. Y. Zhu, R. Paniagua-Domínguez, Y. H. Fu, B. Luk'yanchuk, and A. I. Kuznetsov, Laser Photonics Rev. **9**(4), 412–418 (2015).
[22] Z. e. Bomzon, V. Kleiner, and E. Hasman, Opt. Lett. **26**(18), 1424–1426 (2001).
[23] Z. e. Bomzon, G. Biener, V. Kleiner, and E. Hasman, Opt. Lett. **27**(13), 1141–1143 (2002).
[24] A. Y. Zhu, A. I. Kuznetsov, B. Luk'yanchuk, N. Engheta, and P. Genevet, "Traditional and emerging materials for optical metasurfaces," Nanophotonics (published online).
[25] X. Ni, Z. J. Wong, M. Mrejen, Y. Wang, and X. Zhang, Science **349**(6254), 1310–1314 (2015).
[26] A. Silva, F. Monticone, G. Castaldi, V. Galdi, A. Alù, and N. Engheta, Science **343**(6167), 160–163 (2014).
[27] H. Caner, E. Groner, L. Levy, and I. Agranat, Drug Discovery Today **9**(3), 105–110 (2004).
[28] U. Food and D. Administration, Chirality **4**(5), 338–340 (1992).
[29] E. Hecht, *International Edition* (Addison-Wesley, San Francisco, 2002), Vol. 3.
[30] J. F. James, R. S. Sternberg, and S. A. Rice, Phys. Today **23**(12), 55 (1970).
[31] K. Chaganti, I. Salakhutdinov, I. Avrutsky, and G. W. Auner, Opt. Exp. **14**(9), 4064–4072 (2006).
[32] R. J. Crowley, "Miniature spectrometer system and method," Google Patent No. US 6238348 B1 (2001).
[33] W. Schmidt, J. Biochem. Biophys. Methods **58**(2), 125–137 (2004).
[34] T. J. Loretz, "Blood diagnostic spectrophotometer," Google Patent No. US 4357105 A (1982).
[35] O. Barlev and M. A. Golub, IEEE Photonics Technol. Lett. **28**(5), 577–580 (2015).
[36] O. Barlev and M. A. Golub, Appl. Opt. **54**(19), 6098–6102 (2015).
[37] A. Pors, M. G. Nielsen, and S. I. Bozhevolnyi, Optica **2**(8), 716–723 (2015).
[38] M. Khorasaninejad, W. T. Chen, J. Oh, and F. Capasso, Nano Lett. **16**(6), 3732–3737 (2016).
[39] R. C. Devlin, M. Khorasaninejad, W. T. Chen, J. Oh, and F. Capasso, Proc. Natl. Acad. Sci. U. S. A. **113**, 10473–10478 (2016).
[40] P. Lalanne, S. Astilean, P. Chavel, E. Cambril, and H. Launois, J. Opt. Soc. Am. A **16**(5), 1143–1156 (1999).
[41] M. Khorasaninejad, A. Y. Zhu, C. Roques-Carmes, W. T. Chen, J. Oh, I. Mishra, R. C. Devlin, and F. Capasso, Nano Lett. **16**(11), 7229–7234 (2016).
[42] M. V. Berry, J. Mod. Opt. **34**(11), 1401–1407 (1987).
[43] S. Pancharatnam, presented at the Proceedings of the Indian Academy of Sciences-Section A, 1956.
[44] F. Afshinmanesh, J. S. White, W. Cai, and M. L. Brongersma, Nanophotonics **1**(2), 125–129 (2012).

[45] A. Drezet, C. Genet, and T. W. Ebbesen, Phys. Rev. Lett. **101**(4), 043902 (2008).
[46] M. Benetou, B. Thomsen, P. Bayvel, W. Dickson, and A. Zayats, Appl. Phys. Lett. **98**(11), 111109 (2011).
[47] R. Azzam and A. G. Lopez, J. Opt. Soc. Am. A **6**(10), 1513–1521 (1989).
[48] M. R. Foreman and P. Török, Phys. Rev. A **82**(4), 043835 (2010).
[49] D. Lara and C. Paterson, Opt. Exp. **17**(23), 21240–21249 (2009).
[50] T. Todorov, L. Nikolova, G. Stoilov, and B. Hristov, Appl. Opt. **46**(27), 6662–6668 (2007).
[51] W. T. Chen, P. Török, M. R. Foreman, C. Y. Liao, W.-Y. Tsai, P. R. Wu, and D. P. Tsai, Nanotechnology **27**, 224002 (2016).